

Quadratic Solitons in Singly Resonant Degenerate Optical Parametric Oscillators

M. Nie^{✉†} and S. -W. Huang^{✉*}

Department of Electrical, Computer and Energy Engineering, University of Colorado Boulder, Boulder, Colorado 80309, USA



(Received 7 December 2019; revised manuscript received 19 February 2020; accepted 26 March 2020; published 17 April 2020)

By identifying the similarities between the coupled-wave equations and the parametrically driven nonlinear Schrödinger equation, we show the existence conditions of quadratic solitons in continuous-wave pumped singly resonant degenerate optical parametric oscillators (SRDOPOs). Compared to the previously explored doubly resonant DOPOs, quadratic solitons in SRDOPOs are advantageous in their robustness against perturbations induced by dispersion of the effective third-order nonlinearity and temporal walk-off between the signal and the pump. Terahertz comb bandwidth and femtosecond pulse duration are attainable in an example periodically poled Lithium niobate waveguide resonator in the short-wave infrared. The working principle can be extended to other material platforms, making it a competitive ultrashort pulse and broadband comb source architecture at the mid-infrared spectral range.

DOI: 10.1103/PhysRevApplied.13.044046

I. INTRODUCTION

The mode-locked laser (MLL) and optical frequency comb (OFC) have been the cornerstones and key enabling technologies for many scientific breakthroughs in precision frequency metrology, ultrastable time keeping, extreme light-matter interaction, coherent comb spectroscopy, and other fields [1,2]. Recently, OFC based on the dissipative Kerr soliton (DKS) formation in high- Q cubic nonlinear cavities has emerged as a promising complement to the traditional MLL-based OFC [3–12]. The approach provides a new type of compact OFC with ultrahigh repetition rates in the range of 10–1000 GHz, further expanding the already remarkable scope of OFC applications.

Quadratic nonlinear resonators provide yet another compelling route to OFC generation, through either optical parametric oscillation (OPO) or cavity-enhanced second harmonic generation (SHG). In particular, OPO is intrinsically broadband and tunable, and it extends the OFC to otherwise inaccessible wavelengths including the mid-infrared (MIR) spectral range [1]. Traditionally, OPO-based OFC is generated through synchronous pumping, in which the circulating OPO signal is periodically amplified by a MLL that is synchronized to the OPO cavity. Synchronously pumped degenerate OPOs (DOPOs) based on periodically poled Lithium niobate (PPLN) [13–15] and orientation-patterned gallium arsenide (OP GaAs) [16,17] have all been successfully implemented as viable MIR OFC sources. In addition, a new operational regime of

a near-synchronously pumped DOPO has been observed recently in which temporal simulants are formed through the balance between synchronization timing mismatch and nonlinear pulse acceleration [18].

However, synchronously and near-synchronously pumped OPOs require additional MLLs and associated synchronization electronics, thus generally resulting in increased complexity, large footprint, and high cost for such OPOs. To address the issues, techniques to mode-lock continuous-wave (cw) pumped OPO have been investigated and developed. Early efforts in this research direction focused on active mode-locking with intracavity electro-optic modulator and acousto-optic modulator [19–24]. The first attempts towards the passively mode-locked OPO and OFC generation via quadratic nonlinearity were reported in 2013 and 2014, where the intracavity phase-mismatched SHG was utilized [25,26]. Recent theoretical analysis further showed that OFC based on quadratic soliton formation can be attained through either a cavity-enhanced SHG [27] or a DOPO [28–30] in the doubly resonant (DR) configuration.

On the other hand, quadratic soliton formation in the singly resonant (SR) DOPO configuration has not been demonstrated and analyzed, despite much reduced complexity in device fabrication and wavelength tuning. Here, we theoretically study quadratic soliton formation in a cw-pumped PPLN SRDOPO and show the existence conditions of both high-quality bright quadratic solitons and dark-quadratic-soliton pairs. Terahertz comb bandwidth and femtosecond pulse duration are attainable, with their properties characterized through bifurcation analysis, linear stability analysis, and numerical simulation. We identify the phase-matching condition as the most critical

[†]Mingming.Nie@colorado.edu

^{*}shuwei.huang@colorado.edu

design constant in search for the quadratic soliton in cw-pumped SRDOPOs. It determines not only the parametric pump driving term but also the dispersive effective third-order nonlinearity that perturbs the quadratic solitons in two distinctive ways. Finally, we investigate the quadratic soliton perturbation from dispersive nonlinearity as well as group velocity mismatch (GVM) and develop the suitable strategy to avoid their detrimental effects.

II. THEORETICAL ANALYSIS AND NUMERICAL RESULTS

A. Dispersive effective two-photon absorption and Kerr nonlinearity

The field evolution in the retarded time frame through a cw-pumped SRDOPO (Fig. 1) obeys the coupled equations

$$\frac{\partial A}{\partial z} = \left[-\frac{\alpha_{cs}}{2} - i\frac{k_s''}{2}\frac{\partial^2}{\partial \tau^2} \right] A + i\kappa B A^* e^{-i\Delta k z}, \quad (1)$$

$$\frac{\partial B}{\partial z} = \left[-\frac{\alpha_{cp}}{2} - \Delta k' \frac{\partial}{\partial \tau} - i\frac{k_p''}{2}\frac{\partial^2}{\partial \tau^2} \right] B + i\kappa A^2 e^{i\Delta k z}, \quad (2)$$

and the boundary conditions

$$A_{m+1}(0, \tau) = \sqrt{1 - \theta_s} A_m(L, \tau) e^{-i\delta_s}, \quad (3)$$

$$B_{m+1}(0, \tau) = \sqrt{\theta_p} B_{in}, \quad (4)$$

where A is the signal field envelope, B is the pump field envelope, B_{in} is the cw pump, $\alpha_{cs, p}$ are the propagation losses, Δk is the wave-vector mismatch, $\Delta k'$ is the GVM, $k_{s,p}''$ are the group-velocity dispersions (GVDs), L is the nonlinear cavity length, $\theta_{s,p}$ are the coupler transmission

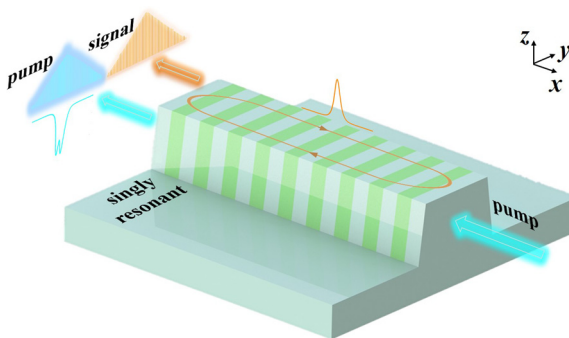


FIG. 1. Schematic of the quadratic soliton mode-locked SRDOPO. The two end faces of the FP cavity are both coated with high transmission at the pump frequency and high reflectivity at the signal frequency. With proper pump and cavity parameters, ultrashort pulses and broadband combs can be generated.

coefficients, and δ_s is the signal-resonance phase detuning [31].

$\kappa = \sqrt{2\omega_0 d_{\text{eff}} / (A_{\text{eff}} \sqrt{c^3 n_s^2 n_p \varepsilon_0})}$ is the normalized second-order nonlinear coupling coefficient, where ω_0 is the center frequency of the signal field, d_{eff} is the effective second-order nonlinear coefficient, A_{eff} is the effective mode area, c is the speed of light, ε_0 is the vacuum permittivity, and $n_{s,p}$ are the linear refractive indices. Higher-order dispersion and nonlinearity are both neglected for simplicity.

Under the mean field, low pump propagation loss, and good cavity approximations [32], Eqs. (1)–(4) can be simplified into a single mean-field equation for the signal field [31]:

$$t_R \frac{\partial A}{\partial t} = \left(-\alpha_s - i\delta_s - i\frac{k_s'' L}{2} \frac{\partial^2}{\partial \tau^2} \right) A - (\kappa L)^2 A^* [A^2 \otimes I(\tau)] + \rho A^*, \quad (5)$$

where t is the “slow time” that describes the envelope evolution over successive round trips, t_R is the round-trip time, τ is the “fast time” that depicts the temporal profiles in the retarded time frame, and α_s is the total signal linear cavity loss. The fourth term on the right-hand side is the effective third-order nonlinearity where the nonlinear response function

$$\hat{I}(\Omega) = \frac{1 - e^{-ix} - ix}{x^2}, \quad (6)$$

and $I(\tau) = \mathcal{F}^{-1}[\hat{I}(\Omega)]$ describes the dispersion of the effective third-order nonlinearity. Here, $x(\Omega) = \xi - D_1 \Omega - D_p \Omega^2$ where Ω is the angular frequency with respect to the signal, $\xi = \Delta k L$ is the wave-vector mismatch parameter, $D_1 = \Delta k L$ is the temporal walk-off, $D_p = k_p'' L / 2$ is the pump group delay dispersion (GDD). The last term on the right-hand side, $\rho = i\kappa L \text{sinc}(\xi/2) e^{-i\xi/2} \sqrt{\theta_p} B_{in}$, is the phase-sensitive parametric pump driving term. Of note, $\xi \neq m2\pi$ ($m \in \mathbb{Z}$, $m \neq 0$) to guarantee a nonzero parametric pump driving term. To shed light on the frequency-dependent nonlinear response function, we separate $\hat{I}(\Omega) = P(\Omega) - iQ(\Omega)$ into the real and imaginary parts to individually examine their effects. Here, $P(\Omega)$ and $Q(\Omega)$ resemble the dispersive two-photon absorption (TPA) and the dispersive Kerr effect, respectively. Importantly, $P(\Omega)$ and $Q(\Omega)$ are set by the choice of the pump parameters and the wave-vector mismatch parameter. We first consider the case of zero GVM ($D_1 = 0$) and then treat GVM as a perturbation to the quadratic soliton in the cw-pumped SRDOPO.

Figure 2 plots the dispersive effective third-order nonlinearity as a function of the wave-vector mismatch parameter ξ . Similarly, Fig. S1 (within the Supplemental Material [33]) plots the dispersive effective third-order nonlinearity as a function of pump GDD D_2 . Two distinct regimes

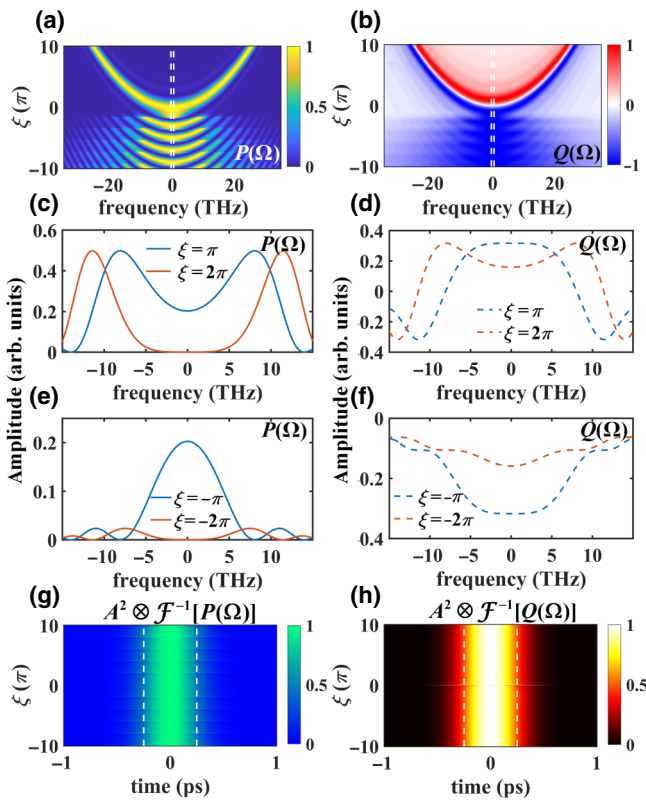


FIG. 2. Frequency response of $P(\Omega)$ (a) and $Q(\Omega)$ (b) as a function of the wave-vector mismatch parameter ξ . Line profiles of $P(\Omega)$ and $Q(\Omega)$ at $\xi = \pm\pi$ and $\xi = \pm 2\pi$ are plotted in (c),(e) and (d),(f), respectively. Influence of ξ on the convolution of the test pulse and inverse Fourier transformation of $P(\Omega)$ and $Q(\Omega)$ are shown in (g) and (h), respectively. The white dashed lines in (a),(b) and (g),(h) depict the test pulse bandwidth and duration, respectively. $L = 15$ mm, $\alpha_p = 0$, $D_1 = 0$ ps, and $D_p = 1222$ fs².

can be evidently identified and divided into the upper zone where $\xi \cdot D_p > 0$ and the lower zone where $\xi \cdot D_p < 0$ [Figs. 2(a) and 2(b)]. The upper zone is characterized by the two resonant effective TPA peaks and the associated nonlinear phase anomalies symmetrically located at $\Omega = \pm\sqrt{\xi/D_p}$. In comparison to DRDOPO, the expression is similar except that the pump detuning is now replaced by the wave-vector mismatch parameter [34]. As the wave-vector mismatch parameter can be set at a much higher value than the pump detuning, SRDOPO is superior to DRDOPO because of the ultrabroad bandwidth of its effective third order nonlinearity. Thus, SRDOPO can support unperturbed soliton with larger bandwidth and tolerate larger walk-off between the pump and signal. In the lower zone, both dispersive effective TPA and dispersive effective Kerr nonlinearity vary periodically with the wave-vector mismatch parameter. Figures 2(e) and 2(f) plot the two extreme profiles of the lower zone $P(\Omega)$ and $Q(\Omega)$, respectively. To elucidate their effect on a pulse, a Gaussian test signal field with a transform-limited pulse

duration ΔT of 500 fs is introduced to convolve with the inverse Fourier transformation of the real and imaginary parts of the nonlinear response function [Figs. 2(g) and 2(h)]. Due to the large bandwidth of $P(\Omega)$ and $Q(\Omega)$, the test pulse does not experience any appreciable time-domain distortion. While the effective TPA manifests itself as the breathing behavior around $\xi = m2\pi$, the effective Kerr nonlinearity manifests itself as the pulse distortion around the phase-matching point.

For the sub-picosecond pulses discussed in this paper, the variation of $P(\Omega)$ and $Q(\Omega)$ over the terahertz bandwidth is less than 1% (Fig. 2). Thus, Eq. (5) can be further simplified into a similar form of the parametrically driven damped nonlinear Schrödinger equation (NLSE) [35,36], by treating $P(\Omega)$ and $Q(\Omega)$ as constant values $P(0)$ and $Q(0)$, respectively:

$$t_R \frac{\partial A}{\partial t} = - \left(\alpha_s + i\delta_s + i \frac{k''L}{2} \frac{\partial^2}{\partial \tau^2} \right) A - \alpha_{\text{TPA}} L |A|^2 A + i\gamma_{\text{eff}} L |A|^2 A + \rho A^*, \quad (7)$$

where $\alpha_{\text{TPA}} = \kappa^2 L P(0) = \kappa^2 L \text{sinc}^2(\xi/2)/2$ is the effective TPA coefficient and $\gamma_{\text{eff}} = \kappa^2 L Q(0) = \kappa^2 L [1 - \text{sinc}(\xi)]/\xi$ is the effective Kerr nonlinear coefficient. Of note, both coefficients can be adjusted through the wave-vector mismatch parameter, the nonlinear cavity crystal length, and the normalized second-order nonlinearity coupling coefficient.

As shown in Fig. 3(a), γ_{eff} can be enhanced from the intrinsic value γ by more than an order of magnitude when ξ is chosen to be between π and 5π . In addition, Fig. 3(b) plots the nonlinear figure of merit (FOM, $\gamma_{\text{eff}}/\alpha_{\text{TPA}}$) as a function of ξ . The oscillatory FOM reaches local maxima and minima at $\xi = m2\pi$ and $\xi = (2n+1)2\pi$ ($n \in \mathbb{Z}$), respectively. Of note, these local maxima cannot be utilized as the parametric pump driving term diminishes at $\xi = m2\pi$. On the other hand, the local minima linearly increase from the phase-matching point with a slope of $\xi/2$.

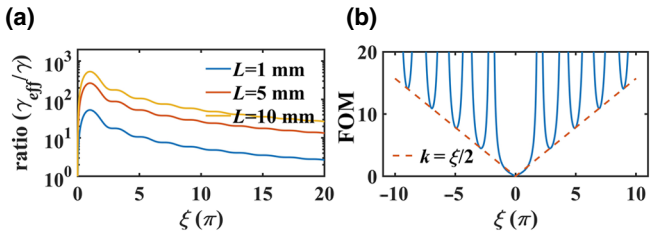


FIG. 3. (a) Enhancement factor of the effective Kerr nonlinearity ($\gamma_{\text{eff}}/\gamma$) as a function of the wave-vector mismatch parameter ξ and the crystal length L in PPLN. The enhancement factor reaches its peak at $\xi = \pi$. (b) Nonlinear FOM ($\gamma_{\text{eff}}/\alpha_{\text{TPA}}$) as a function of the wave-vector mismatch parameter ξ . The local minima linearly increase from the phase-matching point with a slope of $\xi/2$.

$\xi/2$ and thus all the local minima are larger than unity, meaning that the effective Kerr nonlinearity always dominates over the effective TPA. Importantly, wave-vector mismatch parameter ξ is the most critical design constant in the search for the quadratic soliton in the cw-pumped SRDOPO as it determines not only the dispersive third-order nonlinearity but also the parametric pump driving term.

B. Bifurcation and linear stability analysis of the cw solutions

In this subsection, we will analyze the bifurcation behavior of the cw solutions of Eq. (7), including both the trivial (zero) and nontrivial solutions that are also the solutions of Eq. (5). Linear stability analysis using Eq. (7) is developed to study the stable regimes of these solutions [33]. As an example, we choose $\xi = \pm\pi$ such that the parametric pump driving term is a real number. Beside the zero solution, Eq. (7) also has nontrivial cw solutions in the form of $A_0(t, \tau) = |A_0|e^{i\phi}$ with the intracavity power $Y = |A_0|^2$ satisfying:

$$(Yg - \delta_s)^2 + (Y\eta + \alpha_s)^2 = \rho^2, \quad (8)$$

where $g = \pm\kappa^2 L^2 [1 - \text{sinc}(\pi)]/\pi$, $\eta = \kappa^2 L^2 \text{sinc}^2(\pi/2)/2$, $\rho^2 = \kappa^2 L^2 \text{sinc}^2(\pi/2)X$, and pump power $X = |B_m|^2$.

Figure 4 shows the bifurcation diagram of Eq. (8) for the signal at $\xi = \pm\pi$. Linear stability analysis of the zero solution shows that there is a threshold $X_{\text{th}} \equiv (\delta_s^2 + \alpha_s^2)/\kappa^2 L^2 \text{sinc}^2(\pi/2)$ above which the zero solution becomes modulationally unstable (see Section II within the Supplemental Material [33]). In the parameter space where $\xi\delta_s > 0$ and $\xi k_s'' < 0$ (blue lines), the intracavity power exhibits a bistable hysteresis cycle when the pump power falls within $X_{\text{th}} - \Delta X_{\text{th}} < X < X_{\text{th}}$ where $\Delta X_{\text{th}} = [(g\delta_s - \eta\alpha_s)^2/(g^2 + \eta^2)]/[\kappa^2 L^2 \text{sinc}^2(\pi/2)]$. Linear stability analysis of the nontrivial cw solutions shows that the lower branch is modulationally unstable while the upper branch is modulationally stable (section II within the Supplemental Material [33]).

In the parameter space where $\xi\delta_s < 0$ and $\xi k_s'' > 0$ (magenta lines), the intracavity power (only upper branch exists) increases monotonically when the pump is above the threshold. Linear stability analysis of the nontrivial cw

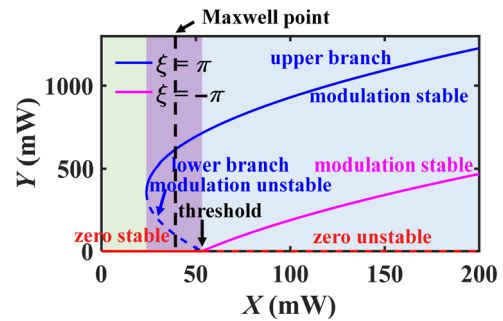


FIG. 4. Bifurcation diagram of Eq. (8) for a subcritical case (blue lines, $\xi\delta_s > 0$ and $\xi k_s'' < 0$) and a supercritical case (magenta lines, $\xi\delta_s < 0$ and $\xi k_s'' > 0$). $g = 0.2105$, $\eta = 0.1340$, $\alpha_s = \pi/160$, and $\delta_s/\alpha_s = 6$.

solutions shows that it is modulationally stable (Section II within the Supplemental Material [33]).

C. Bright soliton

In the simulation, pump power and signal detuning are both scanned in search of the quadratic solitons. Table I summarizes the existence conditions of bright quadratic solitons in a cw-pumped SRDOPO. Equation (7) shows that the sign of the effective Kerr nonlinearity [or g in Eq. (8)] is solely determined by the choice of the wave-vector mismatch ξ such that bright quadratic solitons can exist in both normal and anomalous GVD regimes as long as $\xi k_s'' < 0$. As bright quadratic solitons are formed from the locking of fronts connecting the two stable solutions (the zero solution and the upper-branch solution) [29], they can only exist in the bistable regime (the purple area in Fig. 4) where $X_{\text{th}} - \Delta X_{\text{th}} < X < X_{\text{th}}$ and $\xi\delta_s > 0$.

Finally, dispersion of the effective third-order nonlinearity that perturbs the quadratic solitons further categorizes the bright quadratic solitons into the upper zone where $\xi k_p'' > 0$ and the lower zone where $\xi k_p'' < 0$ [Figs. 2(a) and 2(b)].

By solving Eqs. (1)–(4) with the standard split-step Fourier method, representative pulse shapes and optical spectra of the upper-zone (first row in Table I) and the lower-zone (last row in Table I) bright quadratic solitons are shown in Fig. 5. The bright solitons are excited by writing a 500-fs Gaussian signal pulse for the first 100 iterations and then removing it until the simulation reaches

TABLE I. Existence of bright quadratic soliton with respect to the signs of the wave-vector mismatch parameter, signal GVD, signal-resonance phase detuning, and pump GVD.

Quadratic soliton type	ξ	k_s''	δ_s	k_p''
Upper zone	+	-	+	+
Upper zone	-	+	-	-
Lower zone	+	-	+	-
Lower zone	-	+	-	+

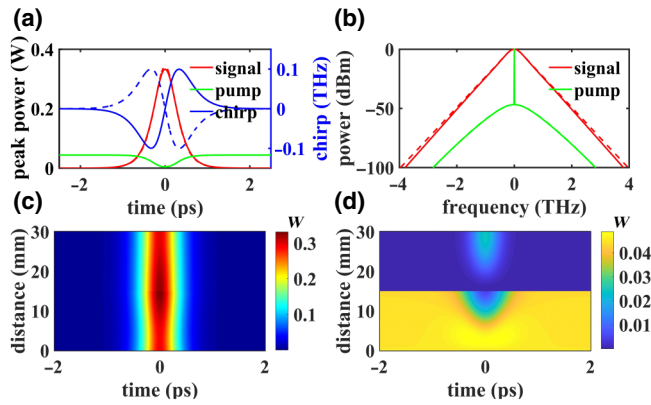


FIG. 5. (a),(b) Pulse shape and optical spectrum of the upper-zone (solid lines) and the lower-zone (dashed lines) bright quadratic soliton in the GV-matched SRDOPO. The pump power $|B_{\text{in}}|^2$ is set below the threshold ($P_{\text{th}} = 53.2$ mW) at 45 mW. The 10-dB comb bandwidth is 0.95 THz and the FWHM pulse duration is 640 fs, slightly chirped from its transform limit of 584 fs. The sign of the chirp depends on the existence branch. Evolution of the upper-zone bright quadratic soliton (c) and the residual pump (d) along the FP cavity. $L = 15$ mm, $t_R = 222$ ps, $\alpha_s = \theta_s = \pi/160$, $\theta_p = 1$, $A_{\text{eff}} = 28 \mu\text{m}^2$, $\kappa = 54.2 \text{ W}^{-1/2} \text{ m}^{-1}$, and $D_p = 1222 \text{ fs}^2$. Upper zone: $\xi = \pi$, $\delta_s / \alpha_s = 6$, and $k_s'' = -325 \text{ fs}^2/\text{mm}$; lower zone: $\xi = -\pi$, $\delta_s / \alpha_s = -6$, and $k_s'' = 325 \text{ fs}^2/\text{mm}$.

a steady state. The dispersive wave at $\Omega = \pm\sqrt{2\Delta k/k_s'}$, resulting from the phase-mismatched nonlinear interaction between the incident pump and the intracavity signal fields, is suppressed by the inclusion of a super-Gaussian filter with a FWHM bandwidth of 20 THz. In both regimes, terahertz comb bandwidth and femtosecond pulse duration are attainable. Both quadratic solitons are stationary in time domain and slightly chirped from its transform limit, with the sign of the chirp depending on the existence regime. Importantly, unlike the DKS-based OFC [3–12], OFC based on quadratic soliton formation in SRDOPO does not have the undesirable cw spectral peak and temporal background. The signal acquires cascaded second-order nonlinearity from the conversion and back-conversion between the pump and signal. The process manifests itself into the pulse-peak power evolution along the propagation distance in the DOPO cavity [Figs. 5(c) and 5(d)].

The parameters used for the upper-zone bright quadratic solitons [solid lines in Figs. 5(a) and 5(b)] can be readily achieved in a monolithic PPLN waveguide Fabry-Perot (FP) resonator with a $28-\mu\text{m}^2$ mode area, a 15-mm length (Fig. S3 within the Supplemental Material [33]), a 1262-nm cw pump wavelength, and a 2524-nm signal center wavelength. Dichroic thin-film coatings with 2% and 100% transmission coefficients at the signal and pump, respectively, are deposited on both the waveguide end surfaces. Due to the large effective Kerr nonlinear coefficient of $14 \text{ W}^{-1} \text{ m}^{-1}$, a high-quality bright quadratic soliton can

be obtained with a cw pump power as low as 45 mW. On the other hand, the existence conditions of lower-zone bright quadratic solitons, $\xi k_s'' < 0$ and $\xi k_p'' < 0$, is much more stringent and it is more challenging to fulfill it in conventional bulk materials and waveguide designs. Multiple zero-dispersion points between the pump and signal wavelengths are required to meet the existence conditions and a strategy to achieve it is by employing a recently studied sandwich waveguide structure [37].

D. Dark soliton

Dark-quadratic-soliton pairs are formed from the locking of two fronts connecting two stable nontrivial cw solutions with identical amplitude but π phase difference. Thus, dark-quadratic-soliton pairs can only exist in: (i) the regime of two upper branches (blue area in Fig. 4) where the solutions above the threshold are modulationally stable; (ii) the regime between the Maxwell point and the threshold where the upper-branch solution is also modulationally stable [29]. Note that the parametric pump driving term ρA^* in Eq. (7) breaks down the continuous phase symmetry $A \rightarrow e^{i\phi}A$ for the undriven case ($\rho = 0$) to the discrete one $A \rightarrow -A$. Thus, the two states of the nontrivial cw solutions are out of phase (with π difference in phase), leading to the formation of the Ising wall (also called the Néel wall) with the form of hyperbolic tangents (also called kinks or dark solitons) [29,38–41].

Here we focus on the dark-quadratic-soliton pair in the first regime where the supercritical upper-branch solution bifurcates from the zero solution and the pump power exceeds the threshold X_{th} (blue area in Fig. 4). Another feature is that the dark solitons must be formed in pairs to satisfy the cavity boundary condition. Figure 6 shows pulse shapes of example dark-quadratic-soliton pairs overlaid with their temporal phase profiles. It can be seen that a dark quadratic soliton consists of two adjacent out-of-phase upper-branch solutions. The pulse duration of the dark quadratic soliton is determined by the signal-resonance phase detuning δ_s and the signal GVD k_s'' . The additional π phase difference between constituent pulses in a dark-quadratic-soliton pair provides the repelling force that stabilizes their separation [38].

III. EFFECT OF WALK-OFF

When the temporal walk-off D_1 is considered, the frequency-dependent nonlinear response function $\hat{I}(\Omega)$ is evidently perturbed and asymmetry occurs in both $P(\Omega)$ and $Q(\Omega)$ as shown in the Fig. 7. In the upper zone where $\xi D_p > 0$, real roots of $\xi - D_1\Omega - D_p\Omega^2 = 0$ can be found and thus two resonant effective TPA peaks and associated nonlinear phase anomalies always exist [Figs. 7(a) and 7(b)]. As the temporal walk-off D_1 increases, the resonance closer to the center frequency ($\Omega = 0$) asymptotically approaches $\Omega = \xi/D_1$ while the other resonance

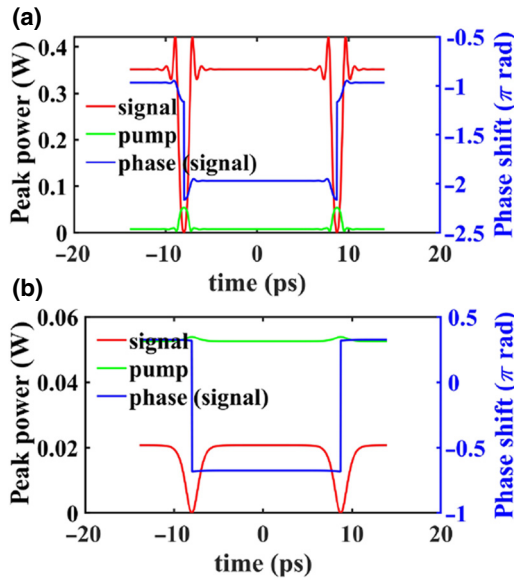


FIG. 6. Existence of dark-quadratic-soliton pairs above the threshold ($P_{\text{th}} = 53.2$ mW) in the GV-matched SRDOPO, with $|B_{\text{in}}|^2 = 55$ mW, $\delta_s/\alpha_s = 6$, and $\xi = \pi$ (a) or $\xi = -\pi$ (b). All the other parameters are the same as in Fig. 5(a).

continues to move away from the center frequency. In comparison to DRDOPO, the expression is similar except that the pump detuning is now replaced by the wave-vector mismatch parameter [34]. As the wave-vector mismatch parameter can be set at a much higher value than the pump detuning, SRDOPO is more robustness against perturbations and can tolerate larger temporal walk-off between pump and signal. In the lower zone where $\xi D_p < 0$, the behavior of the frequency-dependent nonlinear response function is divided into two distinct regimes [Figs. 7(c) and 7(d)]. When the temporal walk-off is small such that $|D_1| < \sqrt{-4\xi D_p}$, there is no real root of $\xi - D_1\Omega - D_p\Omega^2 = 0$ and thus no narrowband resonance phenomenon is present near the center frequency. In this regime, the smooth profiles of $P(\Omega)$ and $Q(\Omega)$ and the relatively large bandwidth guarantee the GVM has minimal perturbative effect to the quadratic soliton. On the other hand, resonant effective TPA peaks and the associated nonlinear phase anomalies reappear as the temporal walk-off increases above $\sqrt{-4\xi D_p}$. Similarly, the resonance closer to the center frequency asymptotically approaches $\Omega = \xi/D_1$.

A straightforward strategy to avoid the detrimental narrowband perturbation is to keep the closer resonance well away from the center frequency by more than the pulse bandwidth, namely $\xi/D_1 \gg 0.315\pi/\Delta T$ (assuming a sech^2 pulse shape), through the choice of a large wave-vector mismatch parameter at the cost of reduced effective Kerr nonlinearity and the parametric pump driving term [see Eq. (7)]. Figure 8 plots the pulse shape and optical spectrum of an upper-zone bright quadratic soliton under

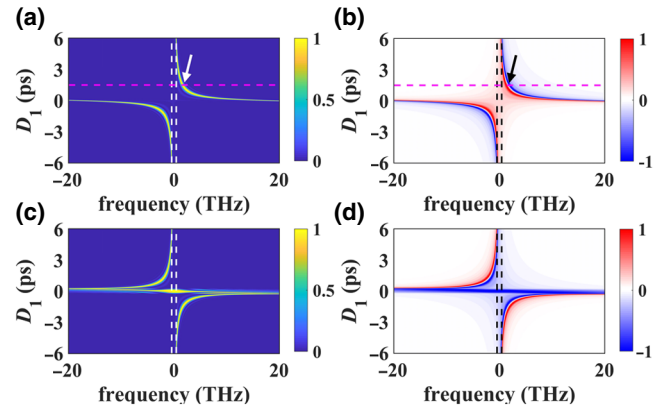


FIG. 7. Effect of temporal walk-off D_1 on the frequency response of $P(\Omega)$ and $Q(\Omega)$ in the upper zone where $\xi = 5\pi$ (a),(b) and the lower zone where $\xi = -5\pi$ (c),(d). The dashed (white and black) lines show the bandwidth of the test pulse. The arrows in (a) and (b) indicate the spectral locations of the resonant TPA peaks and the associated nonlinear phase anomalies. $D_p = 1222$ fs².

a large GVM of $\Delta k'' = 100$ fs/mm and a temporal walk-off of $D_1 = 1.5$ ps. Asymmetry is evidently observed in both the pulse shape and the optical spectrum. One of the spectral peaks of the pump closer to the center frequency is located precisely at the point indicated by the arrows in Figs. 7(a) and 7(b). The temporal walk-off between the signal and the pump manifests itself as the enhanced oscillatory tails on either side of the pump [42], depending on the sign of D_1 . Thus, the corresponding pump spectrum exhibits apparent spectral fringes. Importantly, the signal pulse shape remains clean and minimally perturbed even when the pump is already highly modulated. The bright

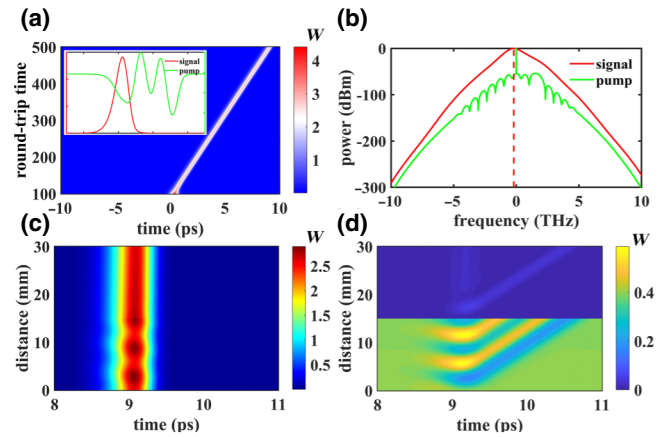


FIG. 8. Pulse shape (a) and optical spectrum (b) of the upper-zone bright quadratic soliton under an increased temporal walk-off of $D_1 = 1.5$ ps. Evolution of the upper-zone bright quadratic soliton (c) and the residual pump (d) along the FP cavity. All the other parameters are the same as in Fig. 5(a), except for $|B_{\text{in}}|^2 = 0.4$ W and $\xi = 5\pi$.

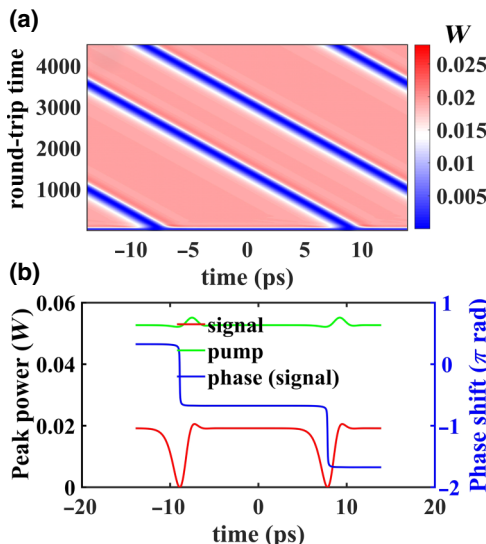


FIG. 9. Time evolution and pulse profile of the dark soliton under an increased temporal walk-off of $D_1 = 1.5$ ps are shown in (a) and (b), respectively. All the other parameters are the same as in Fig. 6(b).

quadratic soliton is stationary in the time domain, but it evolves along the propagation distance in the DOPO cavity as shown in Figs. 8(c) and 8(d) due to the conversion and back-conversion between pump and signal. On the other hand, the pump experiences pulse splitting like soliton fission dynamics [43].

When the GVM $\Delta k''$ and the temporal walk-off D_1 are increased to 160 fs/mm and 2.4 ps, respectively ($\xi/D_1 = \pi/\Delta T$), the perturbation grows so strong that the pulse modulation also builds up in the signal pulse although it remains stable (Fig. S5 within the Supplemental Material [33]). The corresponding pump power requirement is increased to 600 mW. With further increase of the GVM and the temporal walk-off, pulse destabilization eventually occurs, and the bright quadratic soliton ceases to exist in the cw-pumped SRDOPO. As shown in Fig. 9, GVM imposes similar effects on the dark-quadratic-soliton pairs, where dark-quadratic-soliton pairs drift and ripples emerge on one side of the pulses.

IV. CONCLUSIONS

In conclusion, we study the previously unexplored parameter space and unveil the existence conditions of quadratic solitons in cw-pumped SRDOPO. The coupled-wave equations describing the dynamics of SRDOPO can be simplified into a single signal mean-field equation that resembles the parametrically driven NLSE. Bifurcation analysis and linear stability analysis of the cw solutions of the equation identify the origin of quadratic solitons in the cw-pumped SRDOPO as the locking of two modulationally stable solutions. Bright quadratic solitons can exist

in the below-threshold regime exhibiting a bistable behavior, while dark-quadratic-soliton pairs can exist in both the below-threshold and above-threshold regimes, depending on the system parameters. The exact existence condition depends on the interplay between the wave-vector mismatch parameter, the signal GVD, the signal-resonance phase detuning, and the pump GVD.

The dominant perturbation to the quadratic soliton results from the dispersion of the effective third-order nonlinearity; its characteristics can be divided into two distinct branches depending on the sign of the multiplication of the wave-vector mismatch and the signal GDD. In the absence of temporal walk-off, such intrinsic perturbation to the quadratic soliton can be minimized through the choice of a large wave-vector mismatch parameter and small pump GDD. When the temporal walk-off is present, the dispersion of the effective third-order nonlinearity becomes highly asymmetric and the recommended strategy to alleviate the additional GVM perturbation is to increase the wave-vector mismatch parameter.

Numerical simulation confirms that terahertz comb bandwidth and femtosecond pulse duration are attainable in an example PPLN waveguide FP microresonator. The working principle can be further extended to other material platforms, such as CdSiP₂, ZnGeP₂, orientation-patterned (OP-) GaP, and OP GaAs, making it a competitive ultra-short pulse and broadband comb source architecture at the MIR spectral region (3–10 μm).

ACKNOWLEDGMENTS

This work has been supported by the Office of Naval Research (ONR) under Grant No. N00014-19-1-2251. The authors thank Professor Changdong Chen, Dr. Kunpeng Jia, Dr. Bowen Li, and Dr. Xiaohan Wang for fruitful discussions.

- [1] A. Schliesser, N. Picqué, and T. W. Hänsch, Mid-infrared frequency combs, *Nat. Photon.* **6**, 440 (2012).
- [2] N. Picqué and T. W. Hänsch, Frequency comb spectroscopy, *Nat. Photon.* **13**, 146 (2019).
- [3] Y. K. Chembo, Kerr optical frequency combs: Theory, applications and perspectives, *Nanophotonics* **5**, 214 (2016).
- [4] A. A. Savchenkov, A. B. Matsko, and L. Maleki, On frequency combs in monolithic resonators, *Nanophotonics* **5**, 363 (2016).
- [5] S.-W. Huang, J. Yang, M. Yu, et al., A broadband chip-scale optical frequency synthesizer at 2.7×10^{-16} relative uncertainty, *Sci. Adv.* **2**, e1501489 (2016).
- [6] B. Yao, S.-W. Huang, Y. Liu, et al., Gate-tunable frequency combs in graphene-nitride microresonators, *Nature* **558**, 410 (2018).

- [7] Q.-F. Yang, X. Yi, K. Y. Yang, and K. Vahala, Counter-propagating solitons in microresonators, *Nat. Photon.* **11**, 560 (2017).
- [8] S.-W. Huang, A. K. Vinod, J. Yang, et al., Quasi-phase-matched multispectral Kerr frequency comb, *Opt. Lett.* **42**, 2110 (2017).
- [9] Q.-F. Yang, X. Yi, K. Y. Yang, and K. Vahala, Stokes solitons in optical microcavities, *Nat. Phys.* **13**, 53 (2017).
- [10] D. T. Spencer, T. Drake, T. C. Briles, et al., An optical-frequency synthesizer using integrated photonics, *Nature* **557**, 81 (2018).
- [11] T. J. Kippenberg, A. L. Gaeta, M. Lipson, and M. L. Gorodetsky, Dissipative Kerr solitons in optical microresonators, *Science* **361**, eaan8083 (2018).
- [12] A. L. Gaeta, M. Lipson, and T. J. Kippenberg, Photonic-chip-based frequency combs, *Nat. Photon.* **13**, 158 (2019).
- [13] M. Vainio and J. Karhu, Fully stabilized mid-infrared frequency comb for high-precision molecular spectroscopy, *Opt. Express* **25**, 4190 (2017).
- [14] C. Wan, P. Li, A. Ruehl, and I. Hartl, Coherent frequency division with a degenerate synchronously pumped optical parametric oscillator, *Opt. Lett.* **43**, 1059 (2018).
- [15] S. Somekh and A. Yariv, Phase matching by periodic modulation of the nonlinear optical properties, *Opt. Commun.* **6**, 301 (1972).
- [16] N. Leindecker, A. Marandi, R. L. Byer, et al., Octave-spanning ultrafast OPO with 2.6–6.1 μm instantaneous bandwidth pumped by femtosecond Tm-fiber laser, *Opt. Express* **20**, 7046 (2012).
- [17] K. L. Vodopyanov, E. Sorokin, I. T. Sorokina, and P. G. Schunemann, Mid-IR frequency comb source spanning 4.4–5.4 μm based on subharmonic GaAs optical parametric oscillator, *Opt. Lett.* **36**, 2275 (2011).
- [18] M. Jankowski, A. Marandi, C. R. Phillips, et al., Temporal Simultons in Optical Parametric Oscillators, *Phys. Rev. Lett.* **120**, 053904 (2018).
- [19] S. A. Diddams, L.-S. Ma, J. Ye, and J. L. Hall, Broadband optical frequency comb generation with a phase-modulated parametric oscillator, *Opt. Lett.* **24**, 1747 (1999).
- [20] N. Forget, S. Bahbah, C. Drag, et al., Actively mode-locked optical parametric oscillator, *Opt. Lett.* **31**, 972 (2006).
- [21] J. M. Melkonian, N. Forget, F. Bretenaker, et al., Active mode locking of continuous-wave doubly and singly resonant optical parametric oscillators, *Opt. Lett.* **32**, 1701 (2007).
- [22] A. Esteban-Martin, G. K. Samanta, K. Devi, S. C. Kumar, and M. Ebrahim-Zadeh, Frequency-modulation-mode-locked optical parametric oscillator, *Opt. Lett.* **37**, 115 (2012).
- [23] K. Devi, S. C. Kumar, and M. Ebrahim-Zadeh, Mode-locked, continuous-wave, singly resonant optical parametric oscillator, *Opt. Lett.* **37**, 3909 (2012).
- [24] K. Devi, S. C. Kumar, and M. Ebrahim-Zadeh, Directly phase-modulation-mode-locked doubly-resonant optical parametric oscillator, *Opt. Express* **21**, 23365 (2013).
- [25] V. Ulvila, C. R. Phillips, L. Halonen, and M. Vainio, Frequency comb generation by a continuous-wave-pumped optical parametric oscillator based on cascading quadratic nonlinearities, *Opt. Lett.* **38**, 4281 (2013).
- [26] V. Ulvila, C. R. Phillips, L. Halonen, and M. Vainio, High-power mid-infrared frequency comb from a continuous-wave-pumped bulk optical parametric oscillator, *Opt. Express* **22**, 10535 (2014).
- [27] T. Hansson, P. Parra-Rivas, M. Bernard, et al., Quadratic soliton combs in doubly resonant second-harmonic generation, *Opt. Lett.* **43**, 6033 (2018).
- [28] P. Parra-Rivas, L. Gelens, T. Hansson, S. Wabnitz, and F. Leo, Frequency comb generation through the locking of domain walls in doubly resonant dispersive optical parametric oscillators, *Opt. Lett.* **44**, 2004 (2019).
- [29] P. Parra-Rivas, L. Gelens, and F. Leo, Localized structures in dispersive and doubly resonant optical parametric oscillators, *Phys. Rev. E* **100**, 032219 (2019).
- [30] A. Villois, N. Kondratiev, I. Breunig, D. N. Puzyrev, and D. V. Skryabin, Frequency combs in a microring optical parametric oscillator, *Opt. Lett.* **44**, 4443 (2019).
- [31] F. Leo, T. Hansson, I. Ricciardi, et al., Walk-off-induced modulation instability, temporal pattern formation, and frequency comb generation in cavity-enhanced second-harmonic generation, *Phys. Rev. Lett.* **116**, 033901 (2016).
- [32] S. Coen and M. Haelterman, Modulational instability induced by cavity boundary conditions in a normally dispersive optical fiber, *Phys. Rev. Lett.* **79**, 4139 (1997).
- [33] See Supplemental Material at <http://link.aps.org/supplemental/10.1103/PhysRevApplied.13.044046> for the effect of pump GDD on the nonlinear response function, the linear stability analysis of the CW solutions, the design of the PPLN waveguide, and the bright solitons in cavity enhanced SHG.
- [34] M. Nie and S.-W. Huang, Quadratic soliton mode-locked degenerate optical parametric oscillator, *Opt. Lett.* **45**, 2311 (2020).
- [35] S. Longhi, Ultrashort-pulse generation in degenerate optical parametric oscillators, *Opt. Lett.* **20**, 695 (1995).
- [36] I. V. Barashenkov and E. V. Zemlyanaya, Stable complexes of parametrically driven, damped nonlinear Schrödinger solitons, *Phys. Rev. Lett.* **83**, 2568 (1999).
- [37] Y. Guo, Z. Jafari, L. Xu, et al., Ultra-flat dispersion in an integrated waveguide with five and six zero-dispersion wavelengths for mid-infrared photonics, *Photon. Res.* **7**, 1279 (2019).
- [38] I. V. Barashenkov, S. R. Woodford, and E. V. Zemlyanaya, Parametrically Driven Dark Solitons, *Phys. Rev. Lett.* **90**, 054103 (2003).
- [39] G. J. de Valcárcel, I. Pérez-Arjona, and E. Roldán, Domain Walls and Ising-Bloch Transitions in Parametrically Driven Systems, *Phys. Rev. Lett.* **89**, 164101 (2002).
- [40] G.-L. Oppo, A. J. Scroggie, and W. J. Firth, From domain walls to localized structures in degenerate optical parametric oscillators, *J. Opt. B: Quantum Semiclass. Opt.* **1**, 133 (1999).
- [41] G.-L. Oppo, A. J. Scroggie, and W. J. Firth, Characterization, dynamics and stabilization of diffractive domain walls and dark ring cavity solitons in parametric oscillators, *Phys. Rev. E* **63**, 066209 (2001).
- [42] M. Nie, J. Wang, and S.-W. Huang, Solid-state Mamyshev oscillator, *Photon. Res.* **7**, 1175 (2019).
- [43] L. Yin, Q. Lin, and G. P. Agrawal, Soliton fission and supercontinuum generation in silicon waveguides, *Opt. Lett.* **32**, 391 (2007).